AIP | Review of Scientific Instruments

Bulk sensitive hard x-ray photoemission electron microscopy

M. Patt, C. Wiemann, N. Weber, M. Escher, A. Gloskovskii, W. Drube, M. Merkel, and C. M. Schneider

Citation: Review of Scientific Instruments **85**, 113704 (2014); doi: 10.1063/1.4902141
View online: http://dx.doi.org/10.1063/1.4902141
View Table of Contents: http://scitation.aip.org/content/aip/journal/rsi/85/11?ver=pdfcov
Published by the AIP Publishing

Bulk sensitive hard x-ray photoemission electron microscopy

M. Patt,[1,a)] C. Wiemann,[1] N. Weber,[2] M. Escher,[2] A. Gloskovskii,[3] W. Drube,[3] M. Merkel,[2] and C. M. Schneider[1,4]

[1]*Peter Grünberg Institute (PGI-6) and JARA-FIT, Research Center Jülich, D-52425 Jülich, Germany*
[2]*Focus GmbH, Neukirchner Str. 2, D-65510 Hünstetten, Germany*
[3]*DESY Photon Science, Deutsches Elektronen-Synchrotron, D-22603 Hamburg, Germany*
[4]*Fakultät f. Physik and Center for Nanointegration Duisburg-Essen (CeNIDE), Universität Duisburg-Essen, D-47048 Duisburg, Germany*

(Received 24 August 2014; accepted 4 November 2014; published online 26 November 2014)

Hard x-ray photoelectron spectroscopy (HAXPES) has now matured into a well-established technique as a bulk sensitive probe of the electronic structure due to the larger escape depth of the highly energetic electrons. In order to enable HAXPES studies with high lateral resolution, we have set up a dedicated energy-filtered hard x-ray photoemission electron microscope (HAXPEEM) working with electron kinetic energies up to 10 keV. It is based on the NanoESCA design and also preserves the performance of the instrument in the low and medium energy range. In this way, spectromicroscopy can be performed from threshold to hard x-ray photoemission. The high potential of the HAXPEEM approach for the investigation of buried layers and structures has been shown already on a layered and structured $SrTiO_3$ sample. Here, we present results of experiments with test structures to elaborate the imaging and spectroscopic performance of the instrument and show the capabilities of the method to image bulk properties. Additionally, we introduce a method to determine the effective attenuation length of photoelectrons in a direct photoemission experiment. [http://dx.doi.org/10.1063/1.4902141]

I. INTRODUCTION

The rapid evolution of key technological areas, such as information technology, or renewable energy generation and storage is closely connected to a development of new material systems and device structures. The functionality of these device structures, for example, nonvolatile memory cells, spin transistors, photovoltaic elements or batteries is governed by some common aspects. First, the material systems used are rather complex and may involve combinations of intermetallic compounds, multinary oxides, and semiconductors in layered or nanocomposite structures. Second, the actual function and performance is often determined by the quality and the properties of surfaces or interfaces. Third, the relevant processes taking place within the device, for example, a nonvolatile memory cell, during operation may reach down into nanometer length and picosecond time scales.

These circumstances pose particular problems to a characterization of the chemical and electronic states, which forms the basis for an in-depth understanding of the microscopic mechanisms and a further device optimization. In particular, the study of buried interfaces is an important challenge. New characterization methods are needed which should combine chemical selectivity with a sufficiently high information depth and picosecond time-resolution. X-ray photoelectron spectroscopy (XPS) with synchrotron radiation has matured into a very versatile characterization technique in solid state physics and materials science research. It provides convenient access to the electronic states in a sample and yields detailed information about the chemical composition. Aspects related to magnetism and the electron spin have been successfully addressed by exploiting the linear or circular polarization of the synchrotron radiation. Using immersion lens photoelectron microscopes (PEEM), almost all of the above experiments can be carried out with a lateral resolution well below 100 nm. Finally, the well-defined pulse structure of synchrotron radiation provides the means for time-resolved studies down to the 10 ps time scale.[1] The only limitation is the relatively small information depth of less than 1 nm due to the low kinetic energy of the photoelectrons. This is caused by the strong inelastic scattering of the photoelectrons in the sample.[2]

It has been shown, however, that the use of hard x-rays leads to significantly higher escape depths of the photoelectrons, exploiting the dependence of the electron inelastic mean free path (IMFP) on their kinetic energy.[3,4] The great potential of applying the powerful XPS method to electronic and chemical structure investigation of complex bulk materials and multilayered functional device-like structures has led to a rapid evolution of hard x-ray photoelectron spectroscopy (HAXPES) at synchrotron facilities worldwide. Even the feasibility of band structure mapping at several keV energies has recently been demonstrated for high-Z materials, thereby addressing the true bulk electronic band structure of samples.[5] Also very strong magnetic dichroism contrast in core level photoemission from buried magnetic layers has been reported in HAXPES experiments.[6] A pioneering experiment with photoemission microscopy also demonstrated that imaging is possible in the total electron yield mode using excitation with hard x-rays.[7] It was also shown that thick metallic overlayers do not significantly smear out the lateral spatial information carried by fast electrons from buried structures

a)Author to whom correspondence should be addressed. Electronic mail: m.patt@fz-juelich.de. Tel.: +49 2461 61 1486. Current address: Forschungszentrum Jülich GmbH, 52425 Jülich, Germany.

underneath, because of preferential forward scattering at high kinetic energies.[8] In the total electron yield mode, however, element-selectivity can only be introduced by scanning the photon energy across an absorption edge.

Because photoemission spectroscopy gives an easier access and more direct interpretation of chemical bonding states, element-selectivity is more conveniently achieved by energy-filtering of the photoelectrons. We have shown the feasibility of an energy-filtering photoemission microscopy with hard x-rays – which we termed hard x-ray photoemission electron microscope (HAXPEEM) – just recently.[9] In this contribution, we will describe a dedicated energy-filtered photoemission microscope with a high-energy extraction lens which has been optimized for HAXPEEM studies.

II. EXPERIMENTAL SETUP

A. Instrumentation

The HAXPEEM instrument is based on the NanoESCA design introduced in 2005[10] and was modified to extend its operation into the high kinetic energy range up to 10 keV. The heart of the NanoESCA concept is the imaging double hemispherical energy analyzer (IDEA) with compensated analyzer aberrations. This analyzer in combination with a fully electrostatic PEEM optics enables energy-resolved photoemission imaging from the very low energy region close to the photoemission threshold up to typical XPS energies.[11]

For HAXPEEM applications, the electron-optical column of the NanoESCA has been modified. A new lens system operating at a higher extractor voltage ($V_{ext} = 24$ kV) together with an accordingly raised column potential ($V_{col} = 2$ kV) has been implemented. The electron energy transmitted through the energy filter is defined by the sample bias V_{spl}. This biasing scheme enables an easy handling of the imaging column, as all potentials beyond the objective lens, i.e., projective lenses and the energy filter, can be kept at constant conditions during an energy scan. As the extraction field is affected by the sample potential, the extractor voltage has been raised to handle the high kinetic energy electrons. The higher column voltage results in a higher transmission of the microscope using the standard aperture sizes. A second consequence of the higher column voltage is that for energy filtering the retardation of the electrons towards the pass energy of the analyzer must be twice as much as for the standard instrument. Thus, a transfer lens has been implemented behind the objective lens that simultaneously retards and images the electrons towards the first image plane. The standard retardation stage of the microscope can therefore work with the established settings of the standard instrument. The additional lens becomes especially important for high resolution energy filtering which requires analyzer pass energies below 100 eV.

A further consequence of the sample bias is that the microscope's magnification increases with the kinetic energy as the virtual image position of the extracting field shifts towards the objective lens (Fig. 1). During a scan the objective lens is automatically readjusted for the differing energies to be imaged using tabulated lens settings. The automatic control of the focusing voltage over the whole energy range enables wide range spectra and image stacks. The magnification change over the kinetic energy if different core levels are imaged can be taken into account using different final magnifications of the projection lenses. Fig. 2(a) schematically shows the objective lens of the microscope including typical potential settings used for the separate lens parts.

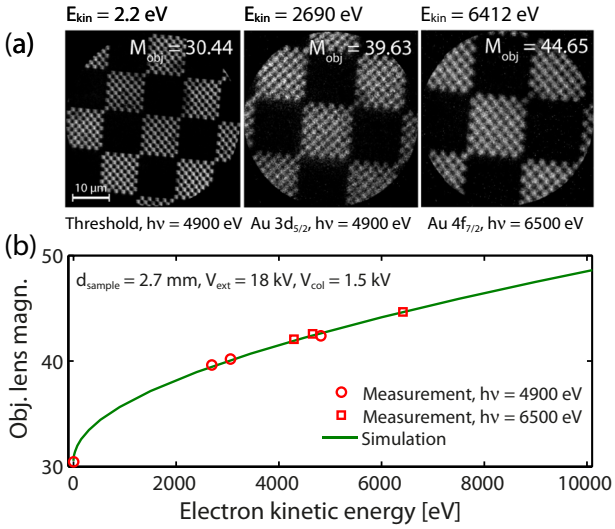

FIG. 1. To analyze the behavior of the objective lens for high kinetic electrons, energy filtered PEEM images of a checkerboard patterned sample were taken for several core levels (Au4f$_{7/2}$, Si 1s, Au3d$_{5/2}$) and for the threshold photoelectrons. Two different photon energies in the hard X-ray regime ($h\nu = 4900$ eV and $h\nu = 6500$ eV) were used. The settings of the projective lenses of the microscope were kept constant, only the focus lens of the objective (see Fig. 2(a)) was adjusted to get a sharp image. The final magnification is a function of the kinetic energy of the electrons. Selected energy-filtered PEEM images are shown in (a). The experimental results acquired with sample distance $d_{sample} = 2.7$ mm, extractor voltage $V_{ext} = 18$ kV, and column potential $V_{col} = 1.5$ kV are shown as dots in (b). They very well fit to the simulated values (solid line) for these settings.

The transmission of the instrument decreases with $1/E_{kin}$, yielding rather small values (see Fig. 3(b)) at high kinetic energies. For photon energies far above atomic ionization thresholds, the photoelectric cross section is generally small and decreases rapidly with energy resulting in low HAXPES

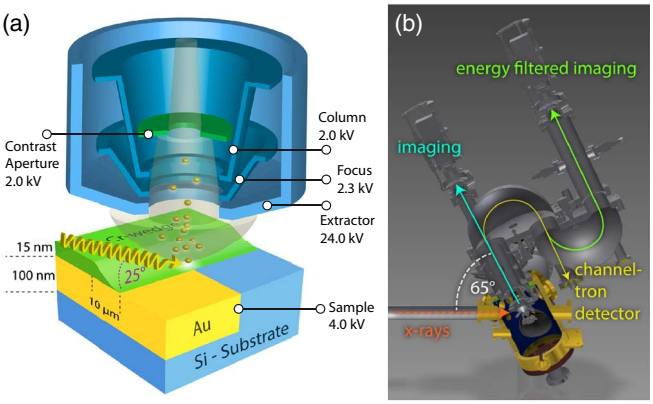

FIG. 2. (a) Schematic setup of the experiment including typical potential settings for the objective lens of the microscope in the high kinetic energy operation mode and a sketch of the wedge-sample design used to measure the thickness dependence of the lateral resolution. (b) Scheme of the HAXPEEM with its energy-filtering hemispheres and different modes of operation. The synchrotron light hits the sample in a 65° angle to the surface normal.

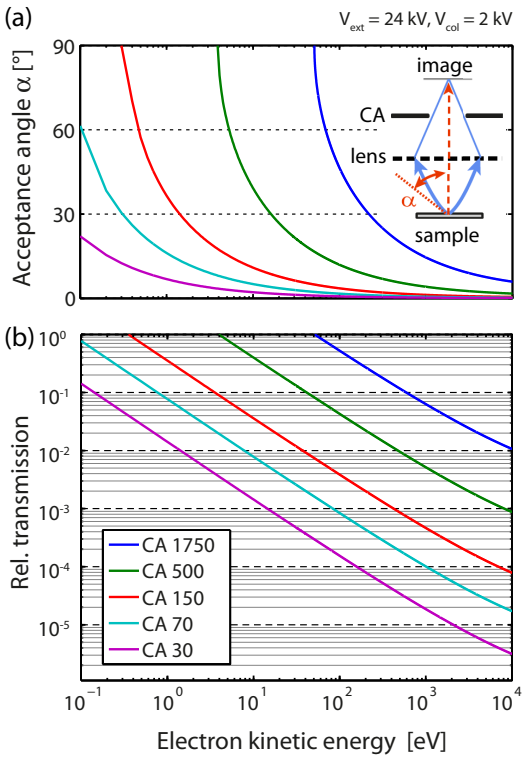

FIG. 3. (a) The microscope's calculated acceptance angle α in the energy-filtered mode as a function of the electron kinetic energy for all available contrast apertures (the diameter of the CAs are indicated). The inset refers to the maximal emission angle α electrons with a specific kinetic energy can have passing the CA. (b) The microscope's transmission characteristics (calculation based on the acceptance angle in (a), see text).

count rates, e.g., for shallow core levels or valence bands. A reasonable signal-to-noise ratio in spectra therefore may require long acquisition times. This in turn asks for an excellent long-time stability of the whole setup, i.e., the instrument and its electronics. In the absence of an optimized hard x-ray micro focus beamline, HAXPEEM must be performed with a rather large contrast aperture (CA), typically 500 μm diameter, in order to reach a sufficiently high instrument transmission. In this regime, the lateral resolution of the instrument is dominated by the spherical aberration of the objective lens. A calculation based on simulated aberration coefficients yields a predicted resolution of approx. 500 nm, consistent with the experimental results reported earlier.[9]

B. Microscope transmission and acceptance angle

A challenge often encountered in photoemission experiments at high photon energies are the rather low signal intensities in comparison to the soft x-ray and ultraviolet regime. In microscopy applications, this effect is even more aggravated by the fact that the usable photon flux is spread over the two-dimensional (2D) field of view. The reason for the signal drop at higher energies is of fundamental nature, as the photoionization cross sections σ_{nl} decrease as $\sigma_{nl}(h\nu) \approx (h\nu)^{-3.5-l}$ (n and l denote the main and angular momentum quantum numbers of the electronic level excited).[12]

Moreover, the electron-optical transmission of the microscope's objective lens decreases in inverse proportion to the kinetic electron energy as

$$T(E_{kin}) = \left(\frac{E_{kin}}{e\ V_{col}} \left(\frac{d_{img} - f_{img}}{r_{CA}\ M} \right)^2 + \frac{E_{kin}}{e\ V_{ext}} \right)^{-1} \quad (1)$$

$$\approx \frac{e\ V_{col}}{E_{kin}} \cdot \left(\frac{r_{CA}\ M}{d_{img} - f_{img}} \right)^2 \quad (2)$$

which derives from electrostatic calculations taking into account the column potential V_{col}, the extractor potential V_{ext}, the objective lens magnification M, the radius r_{CA} of the contrast aperture, and the distance between the focal point and the image plane $d_{img} - f_{img}$ of the objective lens. This transmission behavior relates to the microscope's maximal acceptance angle shown in Fig. 3(a), which can be calculated as

$$\tan(\alpha_{max}) = \left(\frac{E_{kin} \cdot (d_{img} - f_{img})^2}{r_{CA}^2\ e\ V_{col}\ M^2} + \frac{E_{kin}}{e\ V_{ext}} - 1 \right)^{-1/2} \quad (3)$$

and describes the largest starting angle that photoelectrons can have to be completely transmitted through the immersion lens. The transmission in Eq. (1) is finally the integral of the angle-dependent photoelectron intensity distribution $I(\alpha, \phi)$ integrated over the accepted solid angle. Assuming an $I(\alpha, \phi) = \cos(\alpha)$ angular distribution of the excited photoelectrons and an energy-filter width of $\Delta E = 1$ eV we can calculate the transmission values shown in Fig. 3(b) for all available contrast apertures (the diameters are indicated) as a function of the kinetic electron energy. Note, that the magnification M is also a function of the kinetic electron energy so that we used simulated values (like the solid line in Fig. 1(b), but for $d_{sample} = 2.5$ mm, $V_{ext} = 24$ kV, and $V_{col} = 2$ kV) for our calculations. For a CA of 500 μm and electron kinetic energies up to 3.9 eV, the full angular distribution of photoelectrons will be transmitted by the microscope, whereas in the HAXPES regime (e.g., $E_{kin} = 4000$ eV) the calculated transmission drops by a factor of 600.

C. Imaging event counting detector

A new 2D event counting procedure was used with the standard imaging unit of the instrument to improve the signal to noise ratio and the statistical quality of the HAXPEEM measurements presented in Fig. 8. Like it is shown in Fig. 4, photoelectrons reaching the detector are amplified by a multichannel plate (MCP) stack operated in the plateau regime resulting in electron bunches which are accelerated against a YAG scintillator screen. Each electron bunch generates a light signal on the screen at the lateral position of the initial photoelectron. The pattern of events is finally acquired by a 14 bit CCD camera with a frame rate of 53.4 fps. Instead of summing up the light distribution of the screen for a certain exposure time like it is the case in the analog imaging mode, the event counting algorithm maps the separate light events on the screen which were acquired in one frame (18.6 ms minimal exposure time at a frame rate of 53.4 fps, 120 ns interframing time). Each light event is counted as one single event at the lateral coordinates of the center of the light spot. In contrast to the analog imaging, intensity differences caused

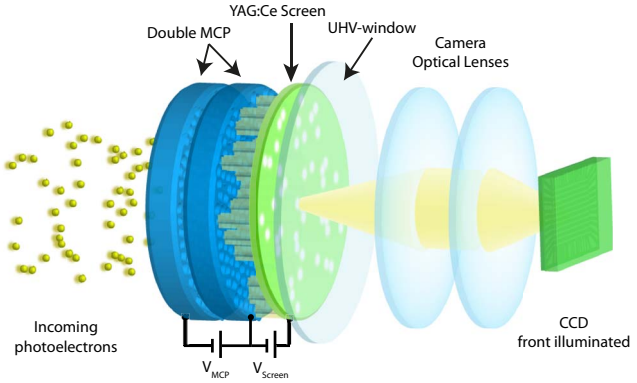

FIG. 4. Sketch of the photoelectron detection system of the microscope as described in the text. The left part works under UHV conditions whereas the fast acquisition camera is placed outside the chamber, separated by a window.

by inhomogeneities in the MCP, the screen, or the CCD are neglected this way. In addition, a spatial signal smear-out of the initial photoelectron event and a cross talk of intensity in high-contrast images, which arises in the MCP, on the screen, and in the camera optics, are suppressed. Only true electron-related events are discriminated and counted. The result is a better signal to noise ratio with less instrumental artifacts and a true Poisson statistic of the electron events as is commonly the case for a channeltron electron multiplier driven counting system used for detection in standard electron energy analyzers. As for all counting systems the count-rate is limited to a maximum rate resulting from the fact that electron events which reach the camera and are acquired in one frame should be clearly separated. With the relatively slow CCD camera used now, the count rate is limited to about 700 kcounts/s. However, this represents no disadvantage, as for higher intensities the camera can be used in an analog mode without any changes in the system setup. Because the photoelectron count rates for the HAXPEEM application are low it is advantageous to use the event counting approach. For quantitative analysis like the EAL determination in Fig. 9 it is even necessary because of its statistical behavior.

D. Sample design

The HAXPEEM experiments were carried out on two types of test samples which were used to address the issues of lateral resolution, chemical selectivity, and information depth.

The first sample type comprises a checkerboard pattern of 100 nm thick gold squares of different sizes on a SiO_2/Si template (see Fig. 1(a)). This commercially available "Chessy" sample (Plano GmbH[13]) has been designed for tests of the lateral resolution and chemical selectivity.

The second sample type mainly addresses the aspects of information depth and lateral resolution. It has been designed to quantify the spatial resolution achievable in imaging of buried structures as a function of the thickness of a cover layer. A sketch of the sample layout is shown in Fig. 2(a). The measurements of the lateral resolution required a laterally defined chemical contrast, which was realized by different adjacent materials with a sharp boundary. Both layers had to be relatively thick (compared to the IMFP in the materials) to obtain a strong bulk signal during the HAXPEEM measurements. Finally, the surface of the pattern had to be smooth to evenly cover it with a thin wedge of Cr. The thickness of the wedge was chosen to increase from 0 nm to 15 nm over a length of approximately 10 μm. This length was chosen to be able to capture the whole wedge in the field of view of the PEEM as well as in an atomic force microscope (AFM).

To fabricate this sample pattern, we used optical lithography and reactive ion beam etching (RIBE) to write approx. 17 μm wide and 100 nm deep channels into a Si-wafer. They were subsequently filled with Au via molecular beam epitaxy (MBE). Afterwards, the structure was planarized via chemical mechanical polishing (CMP). During evaporation of the overlayer, the samples were masked by a knife edge positioned 0.5 mm above the sample surface, resulting in the growth of wedge-shaped cap films. The extensions and profiles of the wedge were determined by AFM. A typical result is shown in Fig. 8(a) as a false-color image and in Fig. 8(b) as a 3D reconstruction. The Au and the Si layers are on nearly the same height and homogeneously covered by the Cr wedge. Only a thin fissure is visible at the Au/Si boundary. The width of this fissure was determined from the AFM data to full-width half-maximum, FWHM = 155 nm, which is significantly below our expected resolution limit of 410 nm determined so far.[9] It will therefore not be visible in the HAXPEEM measurements. The spikes in the AFM data may be related to the CMP process and most likely occur due to particles on the Au surface, whereas the Si surface is usually free of them. It was not possible to remove them by annealing (130 °C, 10 min) or ultrasonic bathing in acetone.

E. Hard x-ray excitation

The HAXPEEM experiments were carried out at the P09 hard x-ray undulator beamline at PETRA-III in Hamburg (Germany).[14] The microscope was installed in the last experiment hutch downstream at about 95 m from the source point. The beamfocus dimensions at this point were determined by fitting a Gaussian distribution to an intensity profile of the beam. The FWHM of the distribution in vertical (horizontal) direction is 382 μm (440 μm). Because the sample-normal in the instrument is tilted by an angle $\alpha = 65°$ against the beam (see Fig. 2) the x-ray footprint on the sample undergoes a geometry smearing by a factor of $\cos(\alpha)^{-1} \approx 2.37$ in the vertical direction compared to the original beam-dimensions. The beamline covers an energy range from 2.7 up to 50 keV with linear polarized light. For the HAXPEEM experiments, the photon energy regime up to 10 keV is most important. Optionally, circularly polarization is also available by means of a diamond phase retarder,[15] but this feature was not yet used in our HAXPEEM studies. The incident photon flux within the 10^{-4} energy bandpass of the Si(111) primary monochromator was about 2×10^{13} s^{-1}.

III. HAXPEEM: RESULTS

A. Bulk sensitive imaging and chemical imaging

The bulk sensitivity of HAXPEEM is demonstrated in a measurement on the Chessy sample mapping the Si 2*p* peak (see Fig. 5). The high kinetic energy spectrum taken at

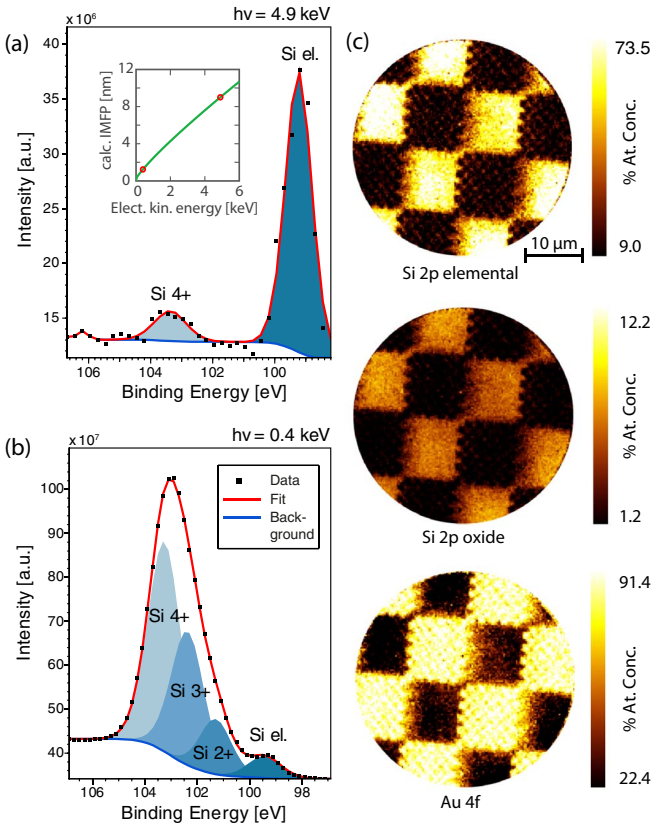

FIG. 5. (a) Si 2*p* spectral distributions obtained with hard x-ray excitation (hv = 4.9 keV, taken at PETRAIII, beamline P09); (b) Si 2*p* spectra with soft x-ray excitation (hv = 400 eV, acquired at the Elettra NanoESCA beamline[16]); the inset shows the IMFP of Si as a function of the kinetic electron energy calculated according to Ref. 18. The energies used in the experiment are marked with red circles. (c) Atomic concentration images using the Si 2*p* and Au 4*f* core level peaks. The data have been evaluated with CasaXPS and principal component analysis (PCA) for noise reduction and separation of spectral contributions according to the oxidation state. Exposure time 8 min/image, energy step 0.25 eV, field of view 38 μm. All spectra were taken with 100 eV pass energy and 1 mm slits, resulting in approx. 0.4 eV energy resolution.

$h\nu = 4.9$ keV (Fig. 5(a)) shows predominantly the signal from elemental silicon and a rather small chemically shifted Si^{4+} peak resulting from the native SiO_2 on the surface. For comparison, a spectrum with soft x-ray excitation of $h\nu = 400$ eV (Fig. 5(b)) was acquired with the same sample and instrument at the Elettra NanoESCA beamline.[16] The soft x-ray excited spectrum has much higher statistical accuracy because of the larger cross section and instrument transmission and is qualitatively quite different, showing a strong contribution from Si surface oxides. It is noted that the surface was not cleaned in any way in both experiments. The spectrum can be fitted by a set of spectral lines corresponding to the mixture of different oxidation states of silicon. The fit results are compiled in Table I. The spectral difference of the hard and soft x-ray photoemission spectra results from the different electron effective attenuation lengths (EALs, which describe the IMFP corrected by elastic scattering effects[17]) at the two kinetic energies. Changing from 400 eV to 4.9 keV photon excitation the IMFP in silicon increases from 12.4 Å to 90.0 Å,[18] i.e., the latter case corresponds to photoemission from the bulk of the sample. The attenuation of the photoemission signal behaves

TABLE I. Fit results of the spectral distributions of the Si 2*p* core level excited with different photon energies as shown in Figs. 5(a) and 5(b). The values underline the bulk-sensitivity of hard-X-ray photoemission experiments in contrast to measurements performed with soft-X-ray excitation.

	$h\nu = 0.4$ keV		$h\nu = 4.9$ keV	
	E_{bin} [eV]	% area	E_{bin} [eV]	% area
Si elem.	99.43	5.18	99.23	88.51
Si^{2+}	101.30	12.70		
Si^{3+}	102.37	32.00		
Si^{4+}	103.25	50.12	103.37	11.49

as $I(t) = I_0 \cdot \exp(-t/\lambda)$, where λ is the material dependent EAL of the electrons and t the path traveled through the material. Using this relation, the bulk Si and oxide signals being 88.5% and 11.5% at 4.9 keV electron energy correspond to a native oxide overlayer thickness of 10.8 Å.

Both spectra were extracted from image stacks which have been acquired as a function of kinetic electron energy. Further analysis of the high kinetic energy data set at 4.9 keV in terms of laterally resolved chemical concentration maps is shown in Fig. 5(c). Here, the contributions of silicon and silicon oxide and their locations can be easily distinguished. The analysis procedure to arrive at these maps is the following: the data stack consisting of images at different kinetic energy points is converted into spectra at each image pixel. These spectra are then fitted using standard XPS analysis software CasaXPS.[19] The fitted local intensities can then be displayed as laterally resolved atomic concentration images.

B. Spatial resolution and space-charge effects

Powerful light sources (like dedicated undulator beamlines) with a high photon flux are essential to obtain adequate signal rates in the HAXPES regime. In microscopy applications, however, the primary intensity can be increased only within certain limits. To understand this we have to keep in mind that due to inelastic scattering processes the highly energetic primary photoelectrons create a cascade of low energy secondary electrons. The higher the kinetic energy of the primary electron the larger is the secondary electron contribution for which the transmission of the immersion lens objective is usually higher. All of these electrons have to pass the immersion lens system as the energy filtering of the photoelectrons takes place only further upstream in the instrument. Very high photocurrent densities can lead to undesirable sample charging or loss of image quality due to space charge effects in the electron optics,[20,21] especially in crossover regions of the electron trajectories, for example, the contrast aperture.

In order to investigate this issue, we performed a couple of resolution tests with different photoelectron intensities entering the microscope column. The results are summarized in Fig. 6. When measuring the test structure shown in Fig. 2(a) with the full photon flux ($\approx 10^{13}$ s^{-1}) on the low energy secondary peak ($E_{kin} = 3.9$ eV) and a contrast aperture of 500 μm it was not possible to find microscope settings to acquire a sharp image. Only by reducing the amount of photoelectrons by either closing the aperture or reducing the primary photon

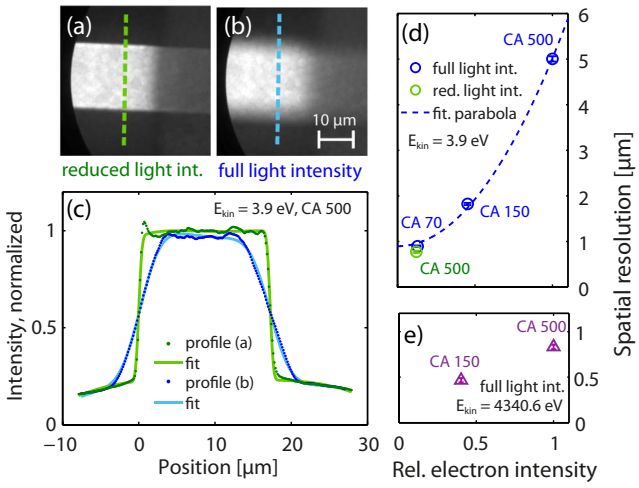

FIG. 6. Depending on the photoelectron current densities inside the microscope the spatial resolution varies significantly. Energy filtered PEEM images of a Au stripe structure were taken for different photon intensities (a) and (b) at the same photon energy $h\nu = 6550$ eV and the same contrast aperture $CA = 500\ \mu$m at the maximum secondary peak $E_{kin} = 3.9$ eV. The line profiles of these measurements were fitted to estimate the resolution (c). Finally, the instrument's spatial resolution was evaluated for various experimental settings at the secondary peak (d). The resolution improves with smaller CA size or a reduction of the photon flux. This suggests that the degradation of lateral resolution is caused by space charge effects within the microscope. The data points could be fitted with a simple parabola $FWHM = a \cdot I^2 + b$. The resolution at high kinetic electron energies is still significantly better (e), because the disturbing secondary electrons are filtered out by the objective lens in this microscope setting (see text).

flux we were able to achieve acceptable spatial resolutions. Fig. 6(a) shows the PEEM image taken with CA = 500 μm and a photon flux which was reduced by beamline filters by a factor of approx. 10. It is possible to achieve a sharp image and to optimize the microscope settings. By removing the filter, the PEEM image becomes significantly blurred, like it is shown in Fig. 6(b). To quantify this change in spatial resolution, a convolution of a step-function with a Gaussian profile was fitted to the intensity profiles (Fig. 6(c)). The overall fit function is

$$I(x) = \left(\frac{I_0}{2} \cdot \left(erf\left(\frac{x - x_1}{\sqrt{2} \cdot \sigma}\right) - erf\left(\frac{x - x_2}{\sqrt{2} \cdot \sigma}\right)\right) + I_{bg}\right) \cdot D(x). \quad (4)$$

The spatial resolution is described by the full-width half-maximum ($FWHM = 2 \cdot \sqrt{2\,ln2} \cdot \sigma$) of the Gaussian. The profiles are superimposed by a broad Gaussian function $D(x)$ derived from the non-isochromaticity of the energy filter[11] which was taken into account in the fitting function. From the fitted profile also the maximum intensity I_0 was extracted to have an approximation of the count rate, which we could compare to the count rates at other microscope settings. The dependence of the spatial resolution on the various settings and the related count rate is shown in Fig. 6(d) for the secondary photoelectrons. The spatial resolution improves dramatically by closing the CA. Alternatively, the same resolution can be obtained by reducing the x-ray flux by an equivalent factor. We do not have enough data points for a confident evidence, but the spatial resolution in this space charge regime seems to increase quadratically with the photoelectron intensity. Thus, for high intensity secondary electron imaging, the spatial resolution is not dominated by the beneficial effects of a smaller CA size, but rather by the reduction of the amount of electrons passing through the lens system of the microscope. This probably reduces distortions caused by space-charge effects in the regions where electron trajectories cross in the microscope.

When we measured the same images with photoelectrons filtered at high kinetic energies (Au 3d, $E_{kin} = 4344.4$ eV) a good spatial resolution could be achieved even with the 500 μm CA, as it is shown in Fig. 6(e). The reason is that with typical HAXPEEM settings like the values given in Fig. 2(a) the objective lens serves as a high-pass filter for kinetic electron energies: Slow electrons are not sufficiently accelerated by the electric field between the sample potential V_{spl} and the extractor potential V_{ext} to overcome the retarding field between the extractor and column potential V_{col}. The slowest electrons which pass into the microscope have to have a kinetic energy of $E_{kin} = e \cdot (V_{spl} - V_{col})$, which would be 2000 eV in our exemplary case. The intense low-energy secondary electron background will therefore **not** enter the microscope and thus related space-charge effects are avoided. As a consequence of the high-pass-filter functionality of the objective lens, the primary electron intensity can be further increased when measuring high kinetic energy electrons to shorten the necessary exposure times.

C. Spatial resolution of covered structures

In order to test whether the spatial resolution of photoemission electrons with a high information depth may be deteriorated by the capping layer they are passing, we used the sample design shown in Fig. 2(a), which provides a chemical contrast between Au and Si-stripes and a gradient in thickness of the covering Cr layer. To acquire element-selective HAXPEEM images, we chose to filter on the two different Au core levels shown in Fig. 7. We picked the Au $3d_{5/2}$ core level at a binding energy of $E_{bin} = 2206.5$ eV and the Au $4f_{7/2}$ core level at $E_{bin} = 84.0$ eV. The photon energy was monochromatized by a Si (111) crystal and set to $h\nu = 6550$ eV, yielding a sufficient energy resolution ($\Delta(h\nu) = 700$ meV) with a comparatively good bulk sensitivity. The photoelectrons collected had kinetic energies of $E_{kin} = 4339.7$ eV (Au $3d_{5/2}$) and $E_{kin} = 6462.2$ eV (Au $4f_{7/2}$). The spectra shown in Fig. 7 were acquired with the channeltron behind the first hemisphere (see Fig. 2(b)). To reach a high microscope transmission, we selected a contrast aperture of CA = 500 μm, a filter pass energy of $E_{Pass} = 100$ eV, and an entrance-slit width of 2 mm, which results in an energy-filter resolution of ($\Delta E_{Inst} = 800$ meV). All measurements were performed at room temperature. The overall energy resolution can be estimated as

$$\Delta E = \sqrt{\Delta(h\nu)^2 + \Delta E_{Inst}^2} = 1063\ \text{meV}. \quad (5)$$

The spectra shown in Fig. 7 have been corrected by subtracting a Shirley-type background and have subsequently been fitted with Voigt profiles. The areas beneath the Au $3d_{5/2}$ and the Au $4f_{7/2}$ peaks differ by a factor of 36.24, the peak heights by a factor of 15.85 due to the lower microscope

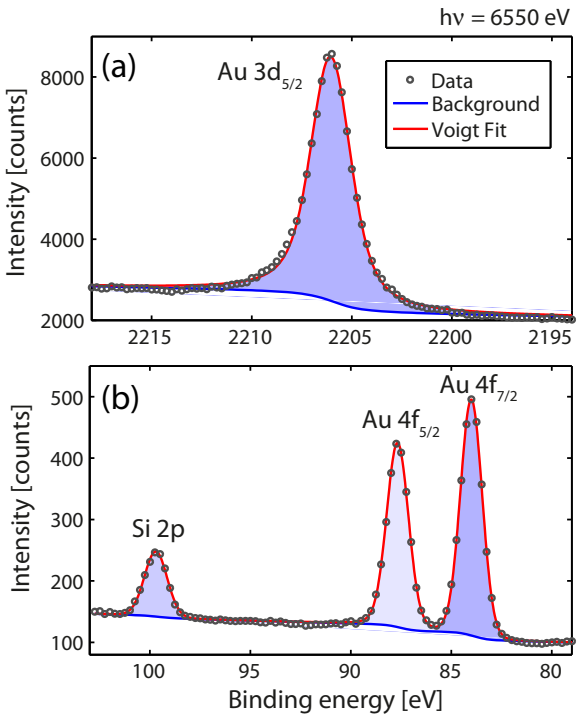

FIG. 7. Au $3d_{5/2}$ core level (a) and Au 4*f* and Si 2*p* core level spectra (b), excited with a photon energy of $h\nu = 6550$ eV. The spectra were measured in the channeltron mode (spatially integrated over the excited sample structure) with different exposure times and normalized for better comparison. The amount of photoelectrons captured from the Au $3d_{5/2}$ is high compared to the Au 4*f* core level and the exposure time for the Au 4*f* core level has to be massively increased.

transmission (compare with Fig. 3(b)) and the lower photoionization cross-section of the Au 4*f* peak at these high photon energies. For the imaging this difference in the count rates is crucial because we collect the electrons from each spatial point of the sample and long acquisition times are needed to obtain reasonable signal-to-noise levels in the contrast. To reach the same statistic from the Au 4*f* core level as from the Au 3*d* core level, one has to expect a factor 16–36 longer exposure time, depending on the energy resolution of the filter. A typical HAXPEEM measurement of the Cr-covered wedge sample is shown in Fig. 8(c) as a false-color plot and as a 3D reconstruction (d). The data were acquired in a single-event counting mode. The data shown in Fig. 8(c) were acquired for 50 min on the Au $3d_{5/2}$ peak. The measured photoelectron intensity can be given in units of single-event counts per camera pixel (counts/px). The photoelectron signal of the uncovered Au region reaches a level of 35.55 counts/px and decreases to a level of 6.85 counts/px in the region where the Cr thickness reaches a value of 16.96 nm. The background level in the Si region is significantly lower. The same experiment was done for photoelectrons descending from the Au $4f_{7/2}$ core level with a three times longer exposure time. The data are shown in Figs. 8(e) and 8(f). Despite the longer exposure time, the maximal measured photoelectron intensity level coming from the uncovered Au is by a factor 3.935 smaller compared to the photoelectrons acquired from the Au $3d_{5/2}$ core level. A 12 times longer exposure time would be needed to achieve equal statistics.

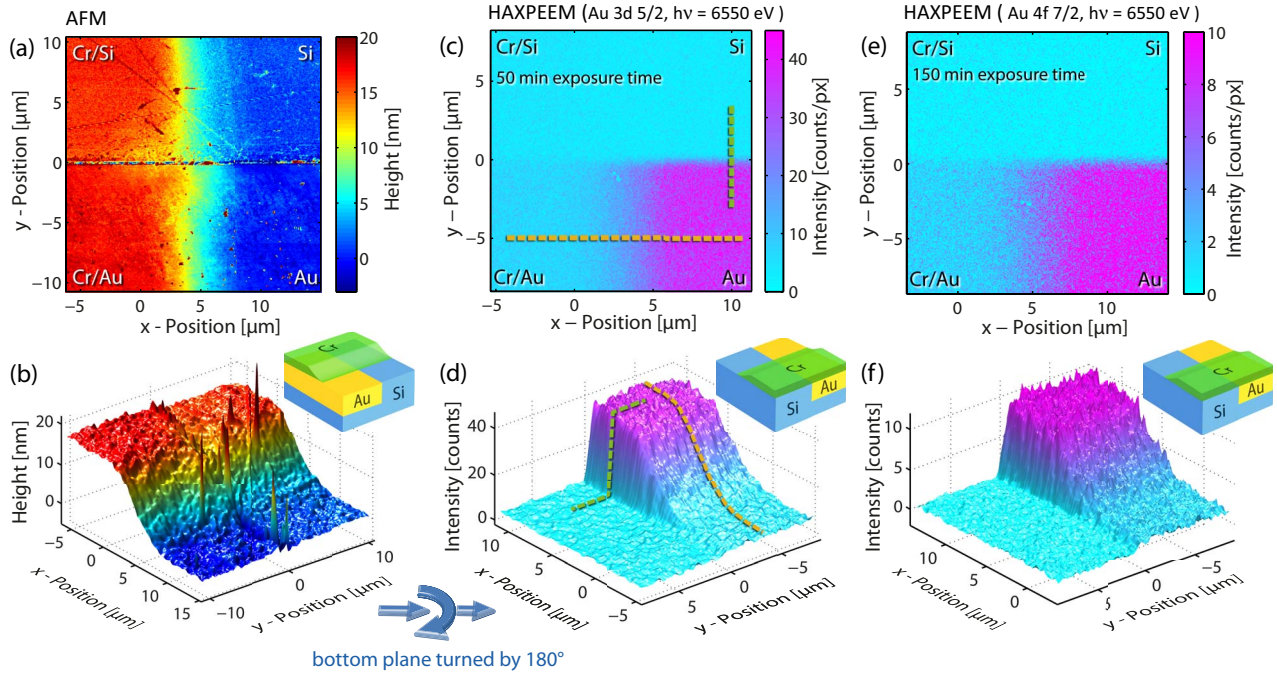

FIG. 8. (a) Atomic force microscopy relief of a manufactured wedge sample. The interface between the Au and the Si layer shows up as a thin fissure. Both materials are nearly on the same height level and are homogeneously covered by the Cr wedge. (b) 3D reconstruction of the AFM data. The spikes indicate polluting particles, probably residuals of the CMP process. They are more prevalent on the Au layer. (c) HAXPEEM image of the wedge on the Au $3d_{5/2}$ peak after 50 min exposure time. The strong Au signal of the uncovered Au stripe vanishes under the Cr wedge. The Si part gives no significant contribution. (d) 3D reconstruction of the HAXPEEM data. The dashed lines indicate the directions along which profiles were taken for the further evaluations. (e) HAXPEEM image of the wedge on the Au $4f_{7/2}$ peak after 150 min exposure time and (f) the related 3D reconstruction. The Au $4f_{7/2}$ signal is significantly lower than the Au $3d_{5/2}$ so that much longer exposure times are needed to reach similar statistics.

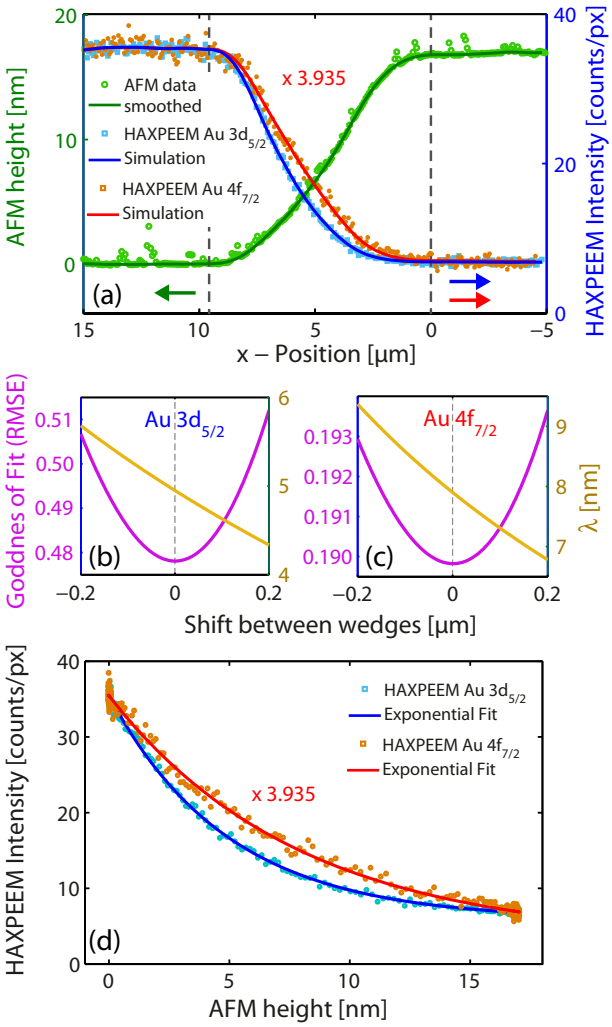

FIG. 9. (a) Comparison between the AFM (green dots) profile representing the Cr wedge and the HAXPEEM (blue and red squares) data for photoelectrons filtered on two different kinetic electron energies. The photoelectron intensities from the Au $4f_{7/2}$ core level were multiplied by a factor of 3.935 so that the signal of the not covered Au parts are on the same level for both core levels. The AFM profile was smoothed (green line). The HAXPEEM data at any wedge position were then assigned to the height of the Cr wedge, resulting in the exponential curves (d). These curves were fitted with Eq. (6). Using the parameters of these exponential fits to simulate the HAXPEEM signal as a function of the Cr-wedge thickness, the red and blue solid lines in (a) are obtained, which very well fit to the original HAXPEEM data. In order to find the correct alignment between the AFM and HAXPEEM profiles in (a), they were shifted with respect to each other and the quality of the resulting exponential fit was judged by its RMSE, where the minimum marks the best fit (b) and (c). The orange curves show the EALs resulting from the exponential fits as a function of the alignment and reveals how sensitive the result of the EAL is on the correct alignment.

1. EAL determination

To compare the AFM-data (Fig. 8(a)) with the photoemission data (Figs. 8(c) and 8(e)), profiles of both data sets were extracted along the wedge direction (see Fig. 9(a)). For a better statistics, the AFM data were averaged over a 6.5 μm wide stripe perpendicular to the wedge-direction, in case of the HAXPEEM data the averaging stripe had a width of 9.7 μm. To be able to directly assign the HAXPEEM data to the height of the wedge-profile, the AFM data were smoothed (green curve). Obvious spikes not belonging to the wedge profile were neglected. Assigning the HAXPEEM profile to the wedge height given by the AFM profile results in the curve shown in Fig. 9(d) which describes the decay of the photoelectron intensity I as a function of the cover thickness t_{wedge}. This curve can be fitted by

$$I(t_{wedge}) = I_0 \cdot \exp\left(-\frac{t_{wedge}}{\lambda \cdot \cos(\alpha)}\right) + I_{bg}, \qquad (6)$$

where $I_0 + I_{bg}$ is the photoelectron intensity measured on the uncovered Au, I_{bg} is the photoelectron background, and λ is the EAL of the photoelectrons traveling through the cover layer.[22] The $\cos(\alpha)$ term takes into account that photoelectrons with higher emission angles α relative to the surface normal have to travel longer distances through the cover layer. Because of the microscope's small acceptance angles for high kinetic electron energies (Fig. 3(a)), we can explicitly neglect this term together with a variety of other angle-dependent issues.[23] The calculated α_{max} values for the relevant kinetic energies are compiled in Table II together with the fit results. The measured EALs are in good agreement with the IMFP calculated using the modified Bethe equation for electrons with $E_{kin} = 4339.7$ eV ($E_{kin} = 6462.2$ eV, respectively) and Cr with the element-specific parameters given in Ref. 18. The difference between the EAL and the IMFP is extensively described in Ref. 17 and is related to elastic scattering effects of the electrons traveling through the cover layer, which therefore in average exhibit longer trajectories inside the cover layer than the straight distance t_{wedge} in Eq. (6) suggests.[24] Without these effects, the EAL and the IMFP would be identical,[25] whereas with these effects the EAL could be smaller than the related IMFP by up to 30%.[26]

The method described above to determine the EAL for a material and a specific electron kinetic energy is commonly referred to as "overlayer film method." Many experimental uncertainties concerning this method were discussed, including uncertainties in film growth and film-thickness measurements, angular anisotropies in electron transport, atomic reconstruction and intermixing at the substrate/overlayer interface, a lack of film uniformity, and effects of surface excitations.[24] What is more, the above mentioned effect of elastic scattering depends on the film thickness[27] and might even result into a non-exponential dependence of the photoemission signal on the overlayer thickness under certain experimental geometries.[28] The evidence that it is exponential

TABLE II. Results of exponential fits shown in Fig. 9(d) and related calculations. The calculated α_{max} as well as the related objective lens transmission were calculated with Eqs. (3) and (1), the IMFP was calculated according to Ref. 18.

	Au $3d_{5/2}$	Au $4f_{7/2}$
E_{kin} [eV]	4339.7	6462.2
calc. α_{max} [deg]	2.27	1.96
calc. transm.	1.57×10^{-3}	1.17×10^{-3}
I_0 [counts/px]	29.61 ± 0.07	8.21 ± 0.05
I_{bg} [counts/px]	5.84 ± 0.07	0.80 ± 0.06
λ [nm]	4.95 ± 0.05	7.90 ± 0.15
calc. IMFP [nm]	5.27	7.35

in our geometry can only be provided by measuring a large variety of different thicknesses which is an inherent feature of our approach. A comparable dense dataset of different film thicknesses can hardly be reached with conventional methods when different samples, one for each overlayer thickness, have to be equally grown and are measured with a non-imaging approach like HAXPES. Using the HAXPEEM approach it is now possible to measure the impact of an overlayer thickness gradient on the photoemission signal of an underlying film in one shot, which in combination with the AFM measurements gives at least a good control over the overlayer film thickness and ensures homogenous growth conditions for the whole dataset.

Nevertheless, the crucial challenge of the wedge-approach is to find the correct positioning of the individually measured profiles shown in Fig. 9(a) relative to each other. This was ensured by involving the following procedure: After a preliminary adjustment by hand the HAXPEEM profile position was shifted by a few hundred nm against the AFM profile. With each constellation the profiles were assigned to each other and the resulting exponential curves were fitted by Eq. (6) described above. The quality of the individual fits can be described by their root-mean-square error (RMSE). The fit with the smallest RMSE value then is indicative of the best relative orientation of the profiles. Figs. 9(b) and 9(c) show how the RMSE of the exponential fits vary with the tuning of the lateral shift between the profiles shown in Fig. 9(a). It also shows the related EAL derived from the fits and how strong it would differ for a not correct alignment.

After determining the correct fit parameters for the exponential function in Fig. 9(d), we simulated a HAXPEEM profile by using Eq. (6) with the gathered fit parameters (Table II) and the smoothed AFM profile shown in Fig. 9(a) (light green). The calculated curves are shown as blue and red lines in Fig. 9(a) and very well fit to the original HAXPEEM data (blue and red squares) confirming the correct positioning of the profiles.

2. Lateral resolution vs. probing depth

The photoemission data shown in Fig. 8 can be used to analyze how the spatial resolution across the Au/Si interface develops beneath an increasing wedge thickness. The interface profile of the HAXPEEM measurement perpendicular to the wedge direction (green curve in Fig. 8(d)) was fitted with a convolution of a Gauss function and a step function (similar to Eq. (4))

$$I(y) = \left(\frac{I_0}{2} \cdot \left(1 + erf\left(\frac{y - y_1}{\sqrt{2} \cdot \sigma}\right)\right) + I_{bg}\right). \quad (7)$$

The FWHM of the Gauss function gives the lateral resolution of the profile. This resolution was determined for the photoemission signals from both core levels shown in Figs. 8(e) and 8(f) which are different in the kinetic energies of the excited photoelectrons (4339.7 eV, 6462.2 eV). How the interface profile develops according to the thickness of the cover-layer is shown in Fig. 10(a) for the Au $3d_{5/2}$ signal. Even under a Cr cover layer of 13.5 nm the signal-to-noise ratio is good enough to detect the chemical contrast between the Au and the Si layer. The development of the fitted resolution as a function of the wedge thickness is shown in Figs. 10(b) and 10(c). Depending on the absolute number of counts collected, the lateral resolution profiles had to be averaged over a certain distance $d_{average}$ to get a good enough signal-to-noise ratio to fit them. In each data set, a line

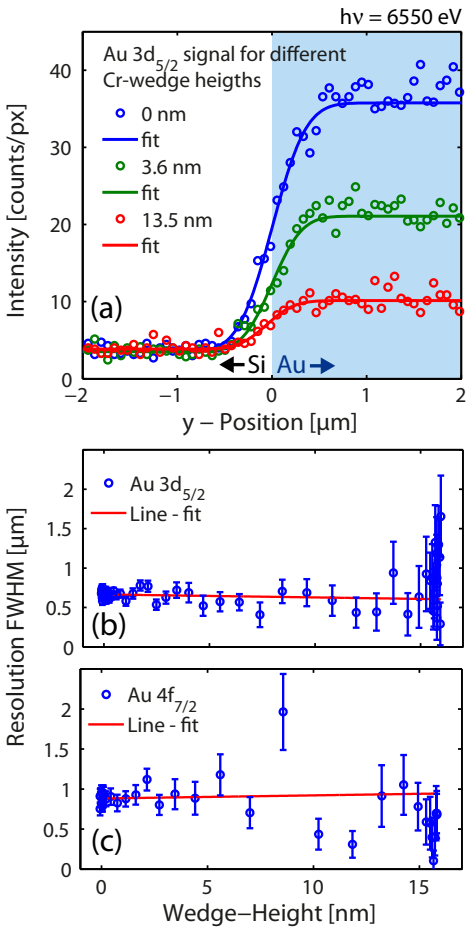

FIG. 10. (a) Profiles extracted from the HAXPEEM data in Fig. 9(c) with different cover thicknesses are fitted to determine the resolution as a function of the cover layer thickness. The results for the Au $3d_{5/2}$ core level are shown in (b) and for the Au $4f_{7/2}$ core level in (c). The Au 4*f* measurements suffer from worse statistic. Nevertheless, both measurements do not show a clear dependance of the spatial resolution with the thickness of the cover layer.

$$FWHM = a \cdot t_{wedge} + b \quad (8)$$

was fitted and the data points were weighted according to their error σ with σ^{-2}. The results are compiled in Table III.

TABLE III. Results of line fits to the resolution measurements shown in Fig. 10.

	Au $3d_{5/2}$	Au $4f_{7/2}$
E_{kin} [eV]	4339.7	6462.2
Wedge length [μm]	9.58	9.58
Integration length [nm]	413	521
a	-4.39 ± 4.06	3.89 ± 14.98
b [nm]	673 ± 9	882 ± 19

The measured spatial resolution for the photoelectrons excited from the Au $3d_{5/2}$ core level seems not to be influenced by a thicker cover layer. The error bars of the fits are nevertheless increasing due to the lower signal-to-noise ratio. The evaluation of the photoelectrons from the Au $4f_{7/2}$ core level was more problematic between a wedge height of 5 nm and 12 nm. The signal-integration along the strong slope of the wedge in combination with a worse initial signal-to-noise ratio restrained the accuracy of the fit procedure. With a flatter slope of the wedge at thicker cover layers the fit results are consistent with the low coverage results. Both line fits have a negligible slope a so that the measured offset b can be interpreted as the measured overall spatial resolution. The overall spatial resolution for the Au $4f_{7/2}$ measurement is worse than for the Au $3d_{5/2}$ measurement due to the fact that the final adjustment of the microscope is more involved with low count rates. Additional experiments showed, that this behavior is not systematically related to the higher kinetic energy of the electrons. Finally we conclude, that in the present experiment, significant changes of the spatial resolution with the thickness of the cover layer are not observed. This issue will be revisited once HAXPEEM data with improved lateral resolution become available.

IV. SUMMARY AND CONCLUSIONS

Based on a commercially available energy filtered photoelectron microscopy concept (NanoESCA), an instrument for HAXPEEM has been designed. We were able to show that in our current resolution limit, the spatial resolution is neither dependent on the thickness of a cover layer nor on its material. Structures on the scale of 500 nm can be imaged without resolution loss even when buried under thicker capping layers. Nevertheless, to prove that really no dependence between spatial resolution and cover layer thickness exists, one will have to do these experiments with a higher instrumental resolution. With the NanoESCA this can be accomplished by using a smaller contrast aperture. However, the next available smaller CA of 150 μm will reduce the count rate by a factor of 10 resulting in unacceptable exposure times in the current experimental configuration. To increase the signal rates, the photon flux density could be enhanced by optimizing the X-ray focus relative to the field of view of the instrument or by using higher extractor potentials, which would lead to larger microscope acceptance angles of the photoelectrons.

Furthermore, we presented a new method to determine the EAL with a direct photo-emission measurement. The measured EALs as a function of the material and the kinetic electron energy are close to calculated IMFPs presented in Ref. 18. The difference between the measured EAL and the IMFP is due to elastically scattered electrons. As we showed in Fig. 3(a) the instrument provides a very narrow acceptance angle for high kinetic electrons, which is useful for this kind of experiments because it allows us to neglect angle-dependent effects for the EAL determination: we are mainly collecting electrons which are crossing the cover layer perpendicular to the surface and do not travel longer distances sideways through the material because of a higher initial angle of the electrons. The combination of microscopic approaches (AFM and HAXPEEM) allows us to gather a reliable dataset of the overlayer thickness dependent photoemission-signals in a one shot experiment, which cancels out doubts in the uniformity of sample growth- and measurement conditions inherent to conventional overlayer film methods.[24] At the same time, the good agreement between EAL measurement and theoretical IMFP prediction proves the applicability of the HAXPEEM for reliable quantitative analysis if the new event counting detection is used.

The evaluation of the HAXPEEM data showed, that we can expect much higher information depths with high kinetic electron energies without a significant loss of spatial resolution, which confirms the conclusions provided in Ref. 8. For future experiments, the best balance between a higher information depth and a shorter acquisition time has to be chosen according to the samples under investigation.

The present study demonstrates the feasibility of the new method as an analytical tool for bulk sensitive chemical and electronic analysis in particular if signal rates can be increased with improved instrumental and X-ray optical parameters. The instrument allows a sub-micrometer resolution and a high probing depth making HAXPEEM a promising technique for the analysis of micro-structured and layered samples, commonly encountered in electronic device engineering.

ACKNOWLEDGMENTS

This work has been supported by the Deutsche Forschungsgemeinschaft (DFG) through SFB 917. The authors would like to thank Silke Kleinen-Göbbels, Rene Borowski, and Michael Schnee (Forschungszentrum Jülich) for help with the wedge-sample construction and analysis as well as Frank Okrent and Heiko Schulz-Ritter (DESY) for the support at the P09 beamline.

[1]F. Nickel, D. M. Gottlob, I. P. Krug, H. Doganay, S. Cramm, A. M. Kaiser, G. Lin, D. Makarov, O. G. Schmidt, and C. M. Schneider, "Time-resolved magnetic imaging in an aberration-corrected, energy-filtered photoemission electron microscope," Ultramicroscopy **130**, 54–62 (2013).

[2]M. P. Seah and W. A. Dench, "Quantitative electron spectroscopy of surfaces: A standard data base for electron inelastic mean free paths in solids," Surf. Interface Anal. **1**(1), 2–11 (1979).

[3]"Proceedings of the workshop on hard x-ray photoelectron spectroscopy: European Synchrotron Radiation Facility, Grenoble, France, September 11–12, 2003," edited by J. Zegenhagen and C. Kunz, Nucl. Instrum. Methods Phys. Res. A **547**(1), 1–238 (2005).

[4]"Recent advances in hard x-ray photoelectron spectroscopy (HAXPES)," edited by W. Drube, J. Electron Spectrosc. Relat. Phenom. **190**, 125–314 (2013).

[5]A. X. Gray, C. Papp, S. Ueda, B. Balke, Y. Yamashita, L. Plucinski, J. Minár, J. Braun, E. R. Ylvisaker, C. M. Schneider, W. E. Pickett, H. Ebert, K. Kobayashi, and C. S. Fadley, "Probing bulk electronic structure with hard x-ray angle-resolved photoemission," Nat. Mater. **10**(10), 759–764 (2011).

[6]X. Kozina, G. H. Fecher, G. Stryganyuk, S. Ouardi, B. Balke, C. Felser, G. Schönhense, E. Ikenaga, T. Sugiyama, N. Kawamura, M. Suzuki, T. Taira, T. Uemura, M. Yamamoto, H. Sukegawa, W. Wang, K. Inomata, and K. Kobayashi, "Magnetic dichroism in angle-resolved hard x-ray photoemission from buried layers," Phys. Rev. B **84**, 054449 (2011).

[7]T. Wakita, T. Taniuchi, K. Ono, M. Suzuki, N. Kawamura, M. Takagaki, H. Miyagawa, F. Guo, T. Nakamura, T. Muro, H. Akinaga, T. Yokoya, M. Oshima, and K. Kobayashi, "Hard x-ray photoelectron emission microscopy as tool for studying buried layers," Jpn. J. Appl. Phys. **45**(3A), 1886 (2006).

[8]T. Kinoshita, E. Ikenaga, J. Kim, S. Ueda, M. Kobata, J. R. Harries, K. Shimada, A. Ino, K. Tamasaku, Y. Nishino, T. Ishikawa, K. Kobayashi,

W. Drube, and C. Kunz, "How is it possible to obtain buried interface information through very thick films using a hard-x-ray peem?," Surf. Sci. **601**(20), 4754–4757 (2007).
[9]C. Wiemann, M. Patt, S. Cramm, M. Escher, M. Merkel, A. Gloskovskii, S. Thiess, W. Drube, and C. M. Schneider, "Probing buried layers by photoelectron spectromicroscopy with hard x-ray excitation," Appl. Phys. Lett. **100**(22), 223106 (2012).
[10]M. Escher, N. Weber, M. Merkel, C. Ziethen, P. Bernhard, G. Schonhense, S. Schmidt, F. Forster, F. Reinert, B. Kromker, and D. Funnemann, "NanoESCA: A novel energy filter for imaging x-ray photoemission spectroscopy," J. Phys.: Condens. Matter **17**(16), S1329–S1338 (2005).
[11]M. Escher, K. Winkler, O. Renault, and N. Barrett, "Applications of high lateral and energy resolution imaging XPS with a double hemispherical analyser based spectromicroscope: Trends in x-ray photoelectron spectroscopy of solids (theory, techniques and applications)," J. Electron Spectrosc. Relat. Phenom. **178–179**, 303–316 (2010).
[12]W. Drube, "Photoelectron spectroscopy with hard x-rays," Nucl. Instrum. Methods Phys. Res. A **547**(1), 87–97 (2005).
[13]Plano GmbH, see http://www.plano-em.de/.
[14]J. Strempfer, S. Francoual, D. Reuther, D. K. Shukla, A. Skaugen, H. Schulte-Schrepping, T. Kracht, and H. Franz, "Resonant scattering and diffraction beamline P09 at PETRA III," J. Synchrotron Radiat. **20**, 541–549 (2013).
[15]S. Francoual, J. Strempfer, D. Reuther, D. K. Shukla, and A. Skaugen, "Double phase-retarder set-up at beamline P09 at PETRA III," J. Phys.: Conf. Ser. **425**(13), 132010 (2013).
[16]C. Wiemann, M. Patt, I. P. Krug, N. B. Weber, M. Escher, M. Merkel, and C. M. Schneider, "A new nanospectroscopy tool with synchrotron radiation: Nanoesca@elettra," e-J. Surf. Sci. Nanotechnol. **9**, 395–399 (2011).
[17]A. Jablonski and C. J. Powell, "Relationships between electron inelastic mean free paths, effective attenuation lengths, and mean escape depths," J. Electron Spectrosc. Relat. Phenom. **100**(1–3), 137–160 (1999).
[18]S. Tanuma, C. J. Powell, and D. R. Penn, "Calculations of electron inelastic mean free paths. IX. Data for 41 elemental solids over the 50 eV to 30 keV range," Surf. Interface Anal. **43**(3), 689–713 (2011).
[19]CasaXPS, 2014, see www.casaxps.com.
[20]A. Locatelli, T. O. Mentes, M. A. Nino, and E. Bauer, "Image blur and energy broadening effects in XPEEM," Ultramicroscopy **111**(8), 1447–1454 (2011).
[21]N. M. Buckanie, J. Göhre, P. Zhou, D. von der Linde, M. Horn-von Hoegen, and F.-J. Meyer zu Heringdorf, "Space charge effects in photoemission electron microscopy using amplified femtosecond laser pulses," J. Phys.: Condens. Matter **21**(31), 314003 (2009).
[22]A. Jablonski and C. J. Powell, "The electron attenuation length revisited," Surf. Sci. Rep. **47**(2–3), 33–91 (2002).
[23]A. Jablonski, M. F. Ebel, and H. Ebel, "Effect of the analyser acceptance angle on the photoelectron intensity," J. Electron Spectrosc. Relat. Phenom. **42**(3), 235–243 (1987).
[24]C. J. Powell and A. Jablonski, "Evaluation of calculated and measured electron inelastic mean free paths near solid surfaces," J. Phys. Chem. Ref. Data **28**(1), 19–62 (1999).
[25]O. A. Baschenko and V. I. Nefedov, "Relative intensities in x-ray photoelectron spectra. Part IX. Estimates for photoelectron mean free paths taking into account elastic collisions in a solid," J. Electron Spectrosc. Relat. Phenom. **27**(2), 109–118 (1982).
[26]C. J. Powell, "Inelastic mean free paths and attenuation lengths of low-energy electrons in solids," Scanning Electron Microsc. **1984/IV**, 1649–1664 (1984).
[27]A. Jablonski, M. F. Ebel, and H. Ebel, "Effects of photoelectron elastic scattering on angular distribution of photoemission from solids," J. Electron Spectrosc. Relat. Phenom. **40**(2), 125–140 (1986).
[28]A. Jablonski and H. Ebel, "Comparison of electron attenuation lengths and escape depths with inelastic mean free paths," Surf. Interface Anal. **11**(12), 627–632 (1988).